

PHASE FIELD FRACTURE IN FIBRE REINFORCED COMPOSITES USING EMBEDDED AND VIRTUAL ELEMENTS

George Pissas*, Savvas P. Triantafyllou*

* National Technical University of Athens

Laboratory of Structural Analysis and Aseismic Research, School of Civil Engineering

Iroon Polytechniou 9, 15772, Athens, Greece

e-mail: {pissasgeorge, savtri}@mail.ntua.gr

www.ntua.gr

Key words: Cohesive Fracture, Continuous Fibre Reinforced Composites, Phase Field

Abstract. Additive manufacturing is emerging as an appealing alternative to standard construction methods, providing capabilities for optimum designs while reducing material usage and construction waste. However, additively manufactured concrete members often come in several non-typical, e.g., tessellated and/or polytope geometries. In this study, a computational framework is developed for the analysis of concrete members reinforced with continuous steel fibres. To this end, a cohesive phase field model is used to simulate fracture in the concrete matrix within a Virtual Element Method (VEM) for the discretization of the resulting coupled system of governing equations. To accurately represent the reinforcement layout while retaining a relatively simple computational model, an embedded element technique is adopted. This combined framework aims at optimizing the discretization processes, overcoming limitations associated with finer mesh requirements while delivering accurate predictions. The effectiveness and robustness of the combined methodology is explored within the context of 2D deformable domains.

1 INTRODUCTION

The increasing demand for stronger, lighter and environmentally aware structures has driven attention towards Additive Manufacturing (AM) technologies. This is mainly due to the unique possibilities it offers, compared to traditional construction methods. Carbon fibre reinforced polymers (CFRPs), known for their exceptional strength-to-weight ratio and durability, have become a key material in this transition, offering innovative solutions for high-performance applications. CFRPs can be broadly categorized into two main types: those reinforced with chopped fibres, which are ideal for complex geometries and cost-sensitive applications, and those with continuous fibres (Continuous Carbon Fibre Reinforced Poly-

mers - CCFRPs), providing high-performance structural components with tailored properties.

In the 1980s, CCFRPs were industrially used, by adopting the Automated Fibre Placement (AFP) technique [2], which was developed to create multidirectional laminates by depositing fibres and preregs along predefined paths. Despite its advantages, AFP faces limitations regarding material options, shape complexity and high costs. However, recent technological advancements regarding 3D printing have enabled the integration of CCFRPs into additive manufacturing processes [3]. One of the most widely used AM categories is Fused Filament Fabrication (FFF) [4]. In CCFRPs manufactured via FFF, the fibres are typically bonded with a matrix material, often a thermo-

plastic (PLA, nylon, PEEK, etc) through a process of extrusion and heat bonding [5]. The matrix material is heated to a molten state and extruded around the continuous fibres, as the filament is deposited layer by layer. As the specimen cools and solidifies, the thermoplastic matrix hardens, encapsulating the fibres and creating a strong bond between matrix and reinforcement [6].

Nevertheless, additively manufactured composites produced via FFF can often have complex and in cases tessellated geometry, with variable stiffness distribution and heterogeneous and anisotropic mechanical properties [7]. These give rise to combined damage mechanisms (e.g. fibre pull-outs and matrix cracking). Undoubtedly, this critical issue pushes current analysis and design tools (Finite Element Analysis - FEA tools and meshing algorithms) to their limits.

In this work, the isotropic cohesive phase field model introduced in [9] is used to simulate fracture of the concrete matrix. For brevity, a uniaxial phase field formulation is also used to account for damage in the embedded truss elements.

The remainder of this manuscript is organised as follows. In Section 2, the cohesive phase field model is briefly presented. Next, the key methodological components of our implementation are presented in Section 3 including the VEM formulation and the embedded element technique used to account for the fibres. Finally, results from two numerical experiments are presented in Section 4 followed by our concluding remarks.

2 Cohesive Phase Field Model

In the following, the case of the 2D deformable domain Ω shown in Fig. 1_{Top} is considered. The domain is supported along the boundary $\partial\Omega_D$ and is subjected to body forces \mathbf{b} and tractions $\bar{\mathbf{t}}$ along the boundary $\partial\Omega_N$. Furthermore, the domain Ω is cracked along the surface Γ .

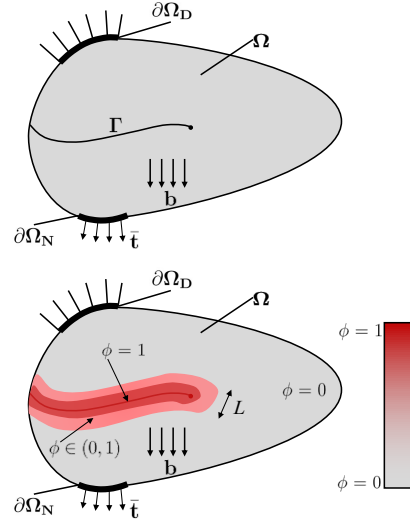


Figure 1: Deformable domain Ω containing: (top) a sharp crack Γ and (bottom) a diffused crack, subjected to body forces \mathbf{b} and Dirichlet and Neumann boundary conditions along $\partial\Omega_D$ and $\partial\Omega_N$ respectively.

2.1 Variational Formulation

Point of departure for the cohesive phase field formulation, is Griffith's variational postulate for Linear Elastic Fracture Mechanics (LEFM) [1]. Within this setting, the potential energy of a cracked solid is represented as the sum of the elastic strain energy and the fracture surface energy as shown in Eq. (1).

$$\begin{aligned} \Pi(\mathbf{u}, \Gamma) = & \int_{\Omega} \psi(\boldsymbol{\varepsilon}(\mathbf{u})) d\Omega + \int_{\Gamma} \mathcal{G}_c d\Gamma \\ & - \int_{\Omega} \mathbf{b} \cdot \mathbf{u} d\Omega - \int_{\partial\Omega_N} \bar{\mathbf{t}} \cdot \mathbf{u} d\partial\Omega_N, \end{aligned} \quad (1)$$

where ψ is the elastic strain energy density, $\boldsymbol{\varepsilon}$ is the linearized strain tensor, \mathbf{u} is the displacement vector at any arbitrary point in Ω and \mathcal{G}_c is the critical energy release rate. The linearized strain tensor $\boldsymbol{\varepsilon}$ is defined as:

$$\boldsymbol{\varepsilon} = \nabla^{\text{sym}} \mathbf{u}, \quad (2)$$

where $\nabla^{\text{sym}} = (\nabla + \nabla^T)/2$ is the symmetric gradient operator.

In the variational phase field fracture theory, the sharp crack path Γ is represented by a diffused crack phase field, represented by a scalar parameter $\phi \in [0, 1]$, where $\phi = 1$ corresponds

to a fully cracked state and $\phi = 0$ to a fully intact state of the material. Thus, the corresponding fracture surface energy term from the right-hand side (r.h.s.) of Eq. (1) is approximated by a regularized volume term according to Eq. (3)

$$\int_{\Gamma} \mathcal{G}_c d\Gamma \approx \int_{\Omega} \mathcal{G}_c \gamma(\phi, \nabla \phi) d\Omega, \quad (3)$$

where

$$\gamma(\phi, \nabla \phi) = \frac{3}{4L} \left[\phi + \frac{L^2}{4} \nabla \phi \cdot \nabla \phi \right], \quad (4)$$

is a linear fracture surface energy approximation function, based on [10]. In Eq. (3), L is the length scale, which corresponds to the width of the crack diffusion zone. Taking into account Eqs. 1, 3 and 4, the total potential energy is expressed as:

$$\begin{aligned} \Pi(\mathbf{u}, \phi) &= \int_{\Omega} \psi(\boldsymbol{\varepsilon}(\mathbf{u}), \phi) d\Omega \\ &+ \int_{\Omega} \mathcal{G}_c \gamma(\phi, \nabla \phi) d\Omega \\ &- \int_{\Omega} \mathbf{b} \cdot \mathbf{u} d\Omega - \int_{\partial\Omega_N} \bar{\mathbf{t}} \cdot \mathbf{u} d\partial\Omega_N. \end{aligned} \quad (5)$$

Note that $\psi(\boldsymbol{\varepsilon}(\mathbf{u}), \phi)$ is also a function of the phase field and represents the degraded elastic strain energy density, reflecting the reduction in the solid's stored elastic strain energy as the crack propagates and the dissipated fracture energy increases.

2.2 Material Degradation

In this work, the strain energy density is additively decomposed into active and passive parts (see [11]), such that:

$$\psi(\boldsymbol{\varepsilon}(\mathbf{u}), \phi) = \psi_a(\boldsymbol{\varepsilon}(\mathbf{u}), \phi) + \psi^-(\boldsymbol{\varepsilon}(\mathbf{u})), \quad (6)$$

where only the term ψ_a contributes to fracture and is therefore degraded by the phase field. The active term may generally be written as:

$$\psi_a(\boldsymbol{\varepsilon}(\mathbf{u}), \phi) = g(\phi) \psi^+(\boldsymbol{\varepsilon}(\mathbf{u})), \quad (7)$$

where $g(\phi)$ is a function that quantifies the stiffness reduction and is referred to as the *degradation function*. The choice of this degradation

function governs the coupling between the displacement and the phase field.

Several strategies for decomposing the strain energy density have been established in the literature, with one of the most popular being the so called "Miehe" decomposition based on [12]. This approach considers a split of the elastic strain energy into a tensile (active) and a compressive (passive) part. This is accomplished via a spectral decomposition of the strain tensor as:

$$\begin{aligned} \boldsymbol{\varepsilon} &= \boldsymbol{\varepsilon}^+ + \boldsymbol{\varepsilon}^- \\ \boldsymbol{\varepsilon}^{\pm} &= \langle \lambda_i \rangle^{\pm} \mathbf{n}_i \otimes \mathbf{n}_i, \end{aligned} \quad (8)$$

where the Macaulay brackets denote $\langle x \rangle^{\pm} = (x \pm |x|)/2$, λ_i are the eigenvalues and \mathbf{n}_i the eigenvectors of the strain tensor $\boldsymbol{\varepsilon}$. Following Eq. (8), the strain energy density components are given by Eq. (9)

$$\psi^{\pm} = \frac{1}{2} \lambda_L [\langle \text{tr}(\boldsymbol{\varepsilon}) \rangle^{\pm}] + \mu_L \boldsymbol{\varepsilon}^{\pm} : \boldsymbol{\varepsilon}^{\pm}, \quad (9)$$

where λ_L, μ_L are the Lamé constants.

Following the work of [13], a quadratic degradation function from Eq. (7) is defined as:

$$g(\phi) = \frac{(1 - \phi)^2}{(1 - \phi)^2 + \frac{3}{2} \frac{E \mathcal{G}_c}{\sigma_c^2 L} \phi \bar{g}(\phi)}, \quad (10)$$

where $\bar{g}(\phi) = 1 + p\phi e^{q^2 \phi^2}$, E is Young's modulus of elasticity, σ_c is the critical fracture stress and $p \geq 1, q$ are two parameters controlling shape of the softening stress strain curve. The interest reader may refer to [8] for a discussion on the calibration of these parameters. Geelen et al. [9] further provide the following stability threshold for the length scale

$$L \leq \frac{3}{2(p+2)} \frac{E \mathcal{G}_c}{\sigma_c^2}. \quad (11)$$

2.3 Governing Equations

The governing equations of the problem can be acquired by applying the principle of minimum total potential energy ([14] to the potential defined in Eq. (5), i.e.,

$$\{\mathbf{u}, \phi\} = \text{Argmin}\{\Pi(\mathbf{u}, \phi)\}. \quad (12)$$

Hence, for arbitrary admissible displacement and phase field variations, $\delta \mathbf{u}$ and $\delta \phi$, respectively, the first variation of the energy functional must vanish:

$$\delta \Pi(\mathbf{u}, \phi; \delta \mathbf{u}, \delta \phi) = 0. \quad (13)$$

To determine all configurations $\{\mathbf{u}, \phi\}$ for which the condition of Eq. (13) is met, one has to determine the stationary points of the functional of Eq. (5).

2.3.1 Displacement Field Sub-Problem

The Euler-Lagrange equation for the functional of Eq. (5), with respect to (w.r.t.) the displacement field is established as:

$$\begin{aligned} \frac{\partial \psi(\boldsymbol{\varepsilon}(\mathbf{u}), \phi)}{\partial \mathbf{u}} - \nabla \cdot \frac{\partial \psi(\boldsymbol{\varepsilon}(\mathbf{u}), \phi)}{\partial(\nabla \mathbf{u})} \\ - \frac{\partial(\mathbf{b} \cdot \mathbf{u})}{\partial \mathbf{u}} - \nabla \cdot \frac{\partial(\mathbf{b} \cdot \mathbf{u})}{\partial(\nabla \mathbf{u})} = 0. \end{aligned} \quad (14)$$

Recalling Eq. (2), as well as that the Cauchy stress tensor is given by:

$$\boldsymbol{\sigma} = \frac{\partial \psi}{\partial \boldsymbol{\varepsilon}}, \quad (15)$$

and plugging Eq. (15) into Eq. (14) yields the well-known momentum balance equation of elastostatics:

$$\nabla \cdot \boldsymbol{\sigma} + \mathbf{b} = 0, \quad (16)$$

with the natural boundary condition:

$$\boldsymbol{\sigma} \cdot \mathbf{n} = \bar{\mathbf{t}} \quad \text{on } \partial \Omega_N, \quad (17)$$

where \mathbf{n} is the vector normal to $\partial \Omega_N$.

2.3.2 Phase Field Sub-Problem

The Euler-Lagrange equation for the functional of Eq. (5), w.r.t. the phase field (first and second term of the r.h.s. of Eq. (5)) is written as:

$$\begin{aligned} \frac{\partial \psi(\boldsymbol{\varepsilon}(\mathbf{u}), \phi)}{\partial \phi} - \nabla \cdot \frac{\partial \psi(\boldsymbol{\varepsilon}(\mathbf{u}), \phi)}{\partial(\nabla \phi)} \\ + \mathcal{G}_c \frac{\partial \gamma}{\partial \phi} - \nabla \cdot \left(\mathcal{G}_c \frac{\partial \gamma}{\partial(\nabla \phi)} \right) = 0. \end{aligned} \quad (18)$$

Using Eqs. 4, 6, 7, we compute each term of Eq. (18) individually:

$$\begin{aligned} c_1 &= \frac{\partial \psi(\boldsymbol{\varepsilon}(\mathbf{u}), \phi)}{\partial \phi} \stackrel{(6,7)}{=} g'(\phi) \psi^+(\boldsymbol{\varepsilon}(\mathbf{u})) \\ c_2 &= \mathcal{G}_c \frac{\partial \gamma}{\partial \phi} \stackrel{(4)}{=} \mathcal{G}_c \frac{3}{4L} \\ c_3 &= \mathcal{G}_c \frac{\partial \gamma}{\partial(\nabla \phi)} \stackrel{(4)}{=} \mathcal{G}_c \frac{3}{4L} \frac{L^2}{2} \nabla \phi \\ &\Rightarrow \nabla \cdot (c_3) = \mathcal{G}_c \frac{3}{4L} \frac{L^2}{2} \nabla \cdot \nabla \phi. \end{aligned} \quad (19)$$

Substituting Eqs.19 in Eq. (18) yields the phase field evolution equation in Eq. (20)

$$\frac{3}{4L} \left(1 - \frac{L^2}{2} \nabla \cdot \nabla \phi \right) = \frac{-g'(\phi) \psi^+}{\mathcal{G}_c} = \mathcal{D}_{iso}, \quad (20)$$

subjected to the natural boundary and irreversibility conditions,

$$\begin{aligned} \nabla \phi \cdot \mathbf{n} &= 0 \\ \dot{\phi} &\geq 0, \end{aligned} \quad (21)$$

respectively. The r.h.s. of Eq. (20) is termed *crack-driving force term*. The system of coupled equations 16 and 20, subjected to conditions 17, 21 along with problem-specific Dirichlet boundary conditions where displacement value $\bar{\mathbf{u}}$ is prescribed, give rise to the following strong form of the problem:

$$(\mathcal{S}) \left\{ \begin{aligned} \nabla \cdot \boldsymbol{\sigma} + \mathbf{b} &= 0 \\ \frac{3}{4L} \left(1 - \frac{L^2}{2} \nabla \cdot \nabla \phi \right) &= \mathcal{D}_{iso} \\ \boldsymbol{\sigma} \cdot \mathbf{n} &= \bar{\mathbf{t}} && \text{on } \partial \Omega_N \\ \mathbf{u} &= \bar{\mathbf{u}} && \text{on } \partial \Omega_D \\ \nabla \phi \cdot \mathbf{n} &= 0 && \text{on } \partial \Omega \\ \dot{\phi} &\geq 0. \end{aligned} \right. \quad (22)$$

2.4 Irreversibility constraint

To enforce the necessary irreversibility constraint on the crack formation, i.e., Eq. (21)₂, an Augmented Lagrange Method is adopted. The phase field governing equation, Eq. (22)₂ is rewritten as:

$$\begin{aligned} & \frac{3}{4L} \left(1 - \frac{L^2}{2} \nabla \cdot \nabla \phi \right) - \underbrace{\langle \lambda + \gamma(\phi_{n-1} - \phi) \rangle^+}_{AL_1} \\ & - \underbrace{\langle \lambda + \gamma(1 - \phi) \rangle^-}_{AL_2} = \mathcal{D}_{iso}, \end{aligned} \quad (23)$$

where λ are the Lagrange multipliers, γ is a penalty parameter and ϕ_{n-1} are the phase field values obtained at time $t = t_{n-1}$. In Eq. (23), term AL_1 imposes a penalty whenever the phase field decreases between subsequent time increments, whereas term AL_2 penalizes phase field values $\phi > 1$. The Lagrange multipliers are iteratively updated until convergence.

3 Solution Procedure

In this section, a first order Virtual Element Method (VEM) formulation to solve problem (\mathcal{S}) of Eq. (22) is briefly revisited. For an extensive review of the mathematical aspects of the method as well as numerous engineering applications the reader is referred to [16] and [17].

3.1 Weak Form

Multiplying the strong form Eqs. 22 (while accounting for the Augmented Lagrange form of the phase field equation Eq. (23)) with the test functions $\delta \mathbf{u}$ and $\delta \phi$ and performing integration by parts leads to the following weak form equilibrium equations:

$$\begin{aligned} \mathcal{R}_u &= \int_{\Omega} \boldsymbol{\sigma} \cdot \nabla \delta \mathbf{u} \, d\Omega - \int_{\Omega} \mathbf{b} \cdot \delta \mathbf{u} \, d\Omega \\ & - \int_{\partial\Omega_N} \bar{\mathbf{t}} \cdot \nabla \delta \mathbf{u} \, d\partial\Omega_N \approx 0 \\ \mathcal{R}_\phi &= \int_{\Omega} \mathcal{D} \delta \phi \, d\Omega \\ & + \int_{\Omega} \frac{3}{4L} \left[\delta \phi + \frac{L^2}{2} \nabla \delta \phi \cdot \nabla \phi \right] \, d\Omega \\ & - \int_{\Omega} (AL_1 + AL_2) \delta \phi \, d\Omega \approx 0, \end{aligned} \quad (24)$$

where terms AL_1 and AL_2 are defined in Eq. (23). Equilibrium demands that the set residuals from Eq. (24) be zero. The solution to the weak form Eq. (24) can be obtained by either monolithic or staggered schemes. In this work, a one-pass staggered scheme from [19] is incorporated, where the residuals \mathcal{R}_u and \mathcal{R}_ϕ are alternatively minimized.

3.2 Linear VEM Formulation

In this section, the implemented VEM formulation will be briefly presented. Several mathematical aspects are omitted for the sake of simplicity. The reader is referred to [17, 18, 20, 21] for details.

A spatial discretization $\mathcal{T}(\Omega)$ of the domain of interest Ω is performed, Fig. 2. Point of departure from classical finite element methods, is that the initial domain, Ω , is partitioned into non-overlapping elements Ω_e , of arbitrary polygonal topology, with a boundary $\partial\Omega_e$ consisting of n_E straight edges E_i , $i \in [1, n_E]$. The elements need not be convex. In this work, a first order VEM is formulated, where virtual elements only have nodes at the vertices, Fig. 2. Higher order VEM technologies also exist, where edge as well as domain interior nodes are defined [17].

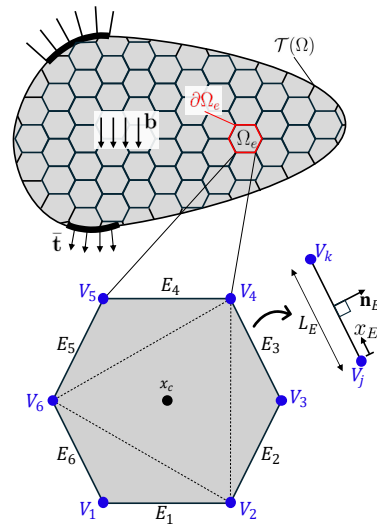


Figure 2: Top: Polygonal discretization $\mathcal{T}(\Omega)$. Bottom: Linear hexagon virtual element.

A key point of the VEM is the additive decomposition of the solution approximations into a projected (polynomial) and a remainder (non-polynomial) part. For the sake of compactness and clarity in the presentation of the formulation, a concise formalism is adopted closely following [17, 20, 21]. The problem is characterized by two primary field variables, namely the displacement and the phase field. The primary field approximations are noted as $\mathfrak{P}_h = \{\mathbf{u}_h, \phi_h\}$. Each primary field is split as:

$$\mathfrak{P}_h = \mathfrak{P}_\pi + (\mathfrak{P}_h - \mathfrak{P}_\pi), \quad (25)$$

where \mathfrak{P}_π is a projection of the primary fields onto a polynomial space; in this case \mathcal{P}_1 . From the definition of appropriate VEM function spaces the primary field ansatz values as well as their gradients cannot be obtained explicitly (see [18]). To tackle this, the presented 2D linear VEM approximates this projection with a linear function w.r.t. the spatial coordinates x, y . This approximation can be written in matrix form as:

$$\begin{aligned} \mathfrak{P}_\pi &= \begin{Bmatrix} u_{\pi x} \\ u_{\pi y} \\ \phi_\pi \end{Bmatrix} = \mathbf{A} \cdot \mathbf{N}_\pi \\ &= \begin{bmatrix} a_1 & a_4 & a_7 \\ a_2 & a_5 & a_8 \\ a_3 & a_6 & a_9 \end{bmatrix} \begin{Bmatrix} 1 \\ x \\ y \end{Bmatrix}, \end{aligned} \quad (26)$$

where $u_{\pi x}, u_{\pi y}$ are the components of the projected part of displacement field in 2D, ϕ_π is the projected part of the phase field variable, $a_i, i = 1 : 9$, are coefficients of the linear approximation to be determined and \mathbf{N}_π is the linear approximation function. The unknown coefficients a_i are computed by employing two conditions. First, one postulates that the primary field ansatz gradients and their corresponding projected parts are orthogonal, i.e.,

$$\int_{\Omega_e} \nabla \mathbf{N}_\pi \cdot (\nabla \mathfrak{P}_h - \nabla \mathfrak{P}_\pi) d\Omega_e, \quad (27)$$

where $\nabla \mathbf{N}_\pi$ is used as a Galerkin weighting function.

Second, the element mean field value of the ansätze and their projection parts are equal, i.e.,

$$\begin{aligned} \int_{\Omega_e} \mathfrak{P}_h d\Omega_e &= \int_{\Omega_e} \mathfrak{P}_\pi d\Omega_e \\ \Rightarrow \sum_{V=1}^{n_V} \mathfrak{P}_h(x_V, y_V) &= \sum_{V=1}^{n_V} \mathfrak{P}_\pi(x_V, y_V), \end{aligned} \quad (28)$$

where n_V is the number of vertices of the virtual element and (x_V, y_V) are the coordinates of each vertex. Eq. (28) holds because of the linear order of the VEM formulation. Furthermore, since the polynomial projection function is of 1st order, the gradient $\nabla \mathbf{N}_\pi = \text{const} \Rightarrow \nabla \mathfrak{P}_\pi = \text{const}$. Following this, and further expanding Eq. (27) yields:

$$\begin{aligned} \nabla \mathbf{N}_\pi \int_{\Omega_e} \nabla \mathfrak{P}_h d\Omega_e &= \nabla \mathbf{N}_\pi \nabla \mathfrak{P}_\pi \Omega_e \Rightarrow \\ \nabla \mathfrak{P}_\pi &= \frac{1}{\Omega_e} \int_{\Omega_e} \nabla \mathfrak{P}_h d\Omega_e. \end{aligned} \quad (29)$$

Using the Gauss theorem for the integral of the r.h.s. of Eq. (29) the following boundary term is obtained:

$$\nabla \mathfrak{P}_\pi = \frac{1}{\Omega_e} \int_{\partial \Omega_e} \mathfrak{P}_h \otimes \mathbf{n}_E d\partial \Omega_e, \quad (30)$$

where \mathbf{n}_E is the vector normal to the element boundary. Recalling the fact that the element boundary comprises n_e straight edges, the flux term from the r.h.s of Eq. (30) is computed over each segment by employing linear 1D finite element shape functions. With reference to Fig. 2_{Bottom}, the primary field ansatz values along an edge E_i are expressed as:

$$\begin{aligned} \mathfrak{P}_h|_{E_i} &= (1 - \xi) \mathfrak{P}_h(x_{V_j}, y_{V_j}) \\ &\quad + \xi \mathfrak{P}_h(x_{V_k}, y_{V_k}), \end{aligned} \quad (31)$$

with V_j, V_k being the start and end nodes of the segment in a counter-clockwise manner and $\xi = x_E/L_E$, the normalized longitudinal local coordinate of edge E_i . Hence, after some algebraic manipulations [17], coefficients $a_i, i = 4 : 9$ can be analytically expressed as a function of the element nodal degrees of freedom (DOFs) according to a relation of the form of Eq. (32):

$$\mathbf{A}_{j:j=4:9} = \mathbb{D}_\nabla \mathfrak{P}(x_V, y_V), \quad (32)$$

where \mathbb{D}_∇ is an analytically defined (for linear VEM) operator, mapping the primary field projected value gradients to the primary field nodal DOFs. Next, the remaining 3 coefficients $a_i, i = 1 : 3$ can be obtained from the condition in Eq. (28) as

$$\mathbf{A}_{j:j=1:3} = \sum_{V=1}^{n_V} [\mathfrak{P}(x_V, y_V) - \nabla \mathfrak{P}_\pi \{x_V \ y_V\}]. \quad (33)$$

Eqs.32, 33 completely define the virtual element projection in terms of the nodal primary field ansatz values.

3.3 Virtual Element State Matrices

Having defined the decomposition of the primary fields Eq. (25), it follows that the total potential energy expression Eq. (5) also assumes a similar form:

$$\Pi(\mathfrak{P}_h) = \Pi_c(\mathfrak{P}_\pi) + \Pi_{stab}(\mathfrak{P}_h - \mathfrak{P}_\pi), \quad (34)$$

where $\Pi_c(\mathfrak{P}_\pi)$ is called the *consistency* part and $\Pi_{stab}(\mathfrak{P}_h - \mathfrak{P}_\pi)$ the *stabilization* part. The stabilization part is necessary since elements with more than 3 vertices based only on the projection part of the primary fields, are rank deficient [18]. Neglecting body and traction forces, the consistency part can be computed for each element by:

$$\begin{aligned} \Pi_c(\mathfrak{P}_\pi) &= \int_{\Omega} \psi(\mathfrak{P}_\pi)|_{x_c} d\Omega \\ &+ \int_{\Omega} \mathcal{G}_c \gamma(\mathfrak{P}_\pi)|_{x_c} d\Omega, \end{aligned} \quad (35)$$

where $\square|_{x_c}$ denotes a quantity that is evaluated at the centroid of the element. It is evident that the residuals of the weak form Eq. (24) can also be written as the sum of a consistency and a stabilization part.

$$\begin{aligned} \mathcal{R}_u &= \mathcal{R}_{u_c} + \mathcal{R}_{u_{stab}} \\ \mathcal{R}_\phi &= \mathcal{R}_{\phi_c} + \mathcal{R}_{\phi_{stab}}. \end{aligned} \quad (36)$$

And in a well known manner the element consistency stiffness matrices, for the displacement and the phase field sub-problems, are given as:

$$\left[\mathbf{K}_{u_c} = \frac{\partial \mathcal{R}_{u_c}}{\partial \mathbf{u}_\pi} \quad \mathbf{K}_{\phi_c} = \frac{\partial \mathcal{R}_{\phi_c}}{\partial \phi_\pi} \right]. \quad (37)$$

With the polynomial part of the solution approximation handled, the non-polynomial (or stabilization) part remains to be defined. According to [22], an energy stabilization strategy is adopted, where the stabilization term of the potential is expressed as:

$$\Pi_{stab}(\mathfrak{P}_h - \mathfrak{P}_\pi) = \hat{\Pi}(\mathfrak{P}_h) - \hat{\Pi}(\mathfrak{P}_\pi), \quad (38)$$

where $\hat{\Pi} = \beta \Pi_c$ is chosen as a scaled consistency potential energy functional. This choice renders the stabilization part computable, however not via the VEM ansatz. To this end, each element polygonal topology, see Fig. 2_{Bottom}, is internally triangulated (there exist many ways to do that [23]) and then regular linear triangular finite elements are employed (see [24]) to compute the element stabilization energy. The work from [20] proposed values for the scaling parameter $\beta \in (0, 1]$. Thus the stability part stiffness matrices for the two sub-problems are computed as:

$$\left[\mathbf{K}_{u_s} = \frac{\partial \mathcal{R}_{u_s}}{\partial \mathbf{u}} \quad \mathbf{K}_{\phi_s} = \frac{\partial \mathcal{R}_{\phi_s}}{\partial \phi} \right]. \quad (39)$$

3.4 Embedded Element Method

In the current work, to account for the fibre reinforcement of the specimens, an embedded element technique is adopted. To this end, the problem domain is defined and discretized with virtual elements. Next, separate 1D line segments are defined within the domain according to the chosen reinforcement pattern (concentric/isotropic [26]). These line segments are not defined in a conforming way to the already computed virtual element mesh, Fig. 3_{Top}. Then a loop over the discretized domain is performed, where every continuum element is checked for intersection with the line segments. If an intersection exists, an embedded element is defined within the host continuum element. The embedded element nodes are defined on the intersections of the boundary with the reinforcement lines. To ensure the interaction between embedded and host elements, a displacement constraint is defined between the generated nodes

and the host element nodes that are on the intersecting boundary edge (see Fig. 3_{Bottom}).

The local stiffness of an embedded truss element, considering longitudinal and transverse displacement nodal DOFs, is

$$\mathbf{K}_{T_e} = \begin{bmatrix} k & 0 & -k & 0 \\ 0 & 0 & 0 & 0 \\ -k & 0 & k & 0 \\ 0 & 0 & 0 & 0 \end{bmatrix}, \quad (40)$$

where $k = E_{T_e} A_{T_e} / L_{T_e}$ is the axial rigidity of the truss element, E_{T_e} is the modulus of elasticity of the reinforcement material, A_{T_e} is the cross-sectional area of the reinforcement and L_{T_e} is the length of the embedded element.

The contribution of the embedded element stiffness to the stiffness of the "composite element" (host & embedded) is computed by:

$$\mathbf{K}_{\mathbf{u}}^{\Omega_e} = \mathbf{K}_{\mathbf{u}}^{\Omega_e} + \mathbf{T}_{\text{emb}}^T \bar{\mathbf{K}}_{T_e} \mathbf{T}_{\text{emb}}, \quad (41)$$

where $\mathbf{K}_{\mathbf{u}}^{\Omega_e}$ is the host virtual element displacement stiffness matrix, $\bar{\mathbf{K}}_{T_e} = \mathbf{T}_{\Lambda}^T \mathbf{K}_{T_e} \mathbf{T}_{\Lambda}$ is the embedded element global stiffness matrix and \mathbf{T}_{Λ} is the element transformation matrix [27].

In Eq. (41), \mathbf{T}_{emb} is a matrix that maps the embedded element nodal DOFs to their corresponding ones at the host element nodes. The dimensions of this matrix depend on the number of vertices, n_V , of the host element. Its entries are computed based on the position of the embedded element node, on the corresponding host element boundary edges.

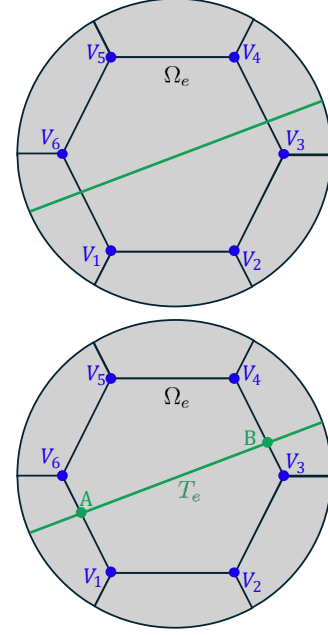


Figure 3: Top: Reinforcement line overlapping with discretization $\mathcal{T}(\Omega)$. Bottom: Embedded truss element definition.

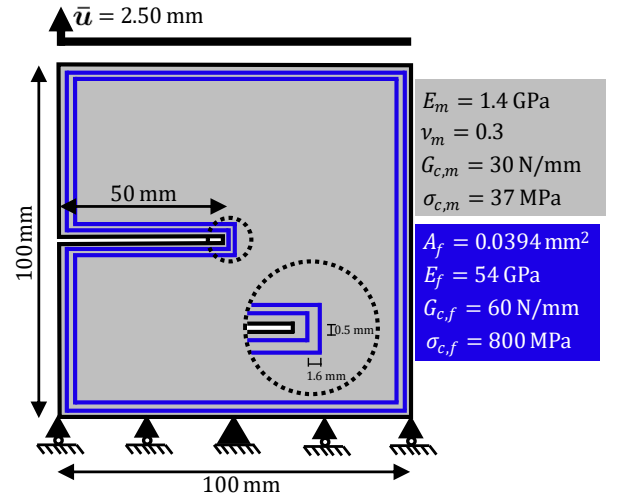


Figure 4: SEN-T: Problem setup.

4 Numerical Experiments

Two applications are presented using the formulation presented in this work. All analyses are performed using an in-house code and have been run on a PC fitted with an Intel i9 processor with 24 cores and 128GB of RAM.

4.1 Single-Edge Notched Specimen under Tension (SEN-T)

A single-edge notched (SEN) 3D printed CCFRP composite specimen is examined. The problem geometry, boundary conditions and reinforcement configuration (in blue) are shown in Fig. 4. Two concentric fibres are defined along the boundary, with a spacing of 1.6 mm. This configuration is termed "CF2". To assess the effect of the reinforcement, a matrix-only model is also considered, termed "CF0". The specimen thickness is 1 mm. The mechanical properties are selected to emulate the properties of a nylon based matrix material called "Onyx" and a continuous carbon fibre filament from Markforged [28]. Values for Young's moduli, Poisson's ratios and energy release rates are based on [29], whereas the critical fracture stress values are obtained from the manufacturer datasheets [28]. The equivalent area of the fibre is computed as:

$$A_f = A_{fil} V_{fil}^{frac}, \quad (42)$$

where A_{fil} is the area of the continuous fibre filament and V_{fil}^{frac} is the filament fibre volume fraction. Following information provided by the manufacturer, the fibre filament diameter is set to 0.38 mm. The filament fibre volume fraction is chosen equal to 35%; numerous works existing in the literature investigate such properties, [30,31]. A displacement equal to 2.5 mm is incrementally imposed on the top edge of the specimen, with an increment $\Delta u = 0.0015$ mm. The domain is discretized with 14793 quadrilateral first-order virtual elements and the length scale value is chosen equal to $L = 1.4$ mm.

Fig. 6 contains the load-displacement curves for configurations CF0 and CF2. The reinforced model is also solved via regular FEM for validation purposes. The inclusion of concentric fibre reinforcement has a negligible effect on the elastic stiffness. However, it results in an 8.3% increase in the ultimate load. Phase field contours for both matrix-only (left column) and reinforced (right column) configurations are illustrated in Fig. 5. Snapshots for three top edge displacement values are displayed in the three

plot rows. It can be observed that, for the CF2 layout, the crack gets arrested on each fibre, resulting in higher strength. This is anticipated as the fibre-strength and toughness are much higher than the corresponding matrix material properties.

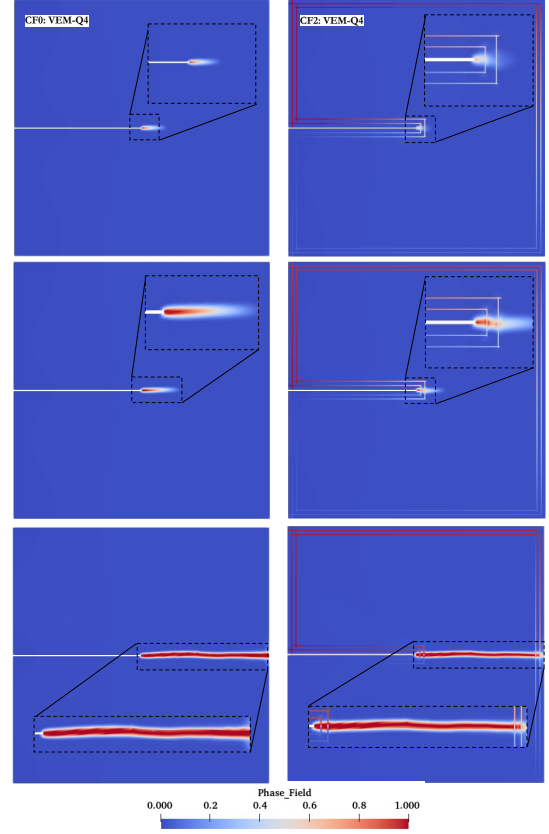


Figure 5: SEN-T: Phase field contour plots for different top edge displacements. Top: 1.8 mm, Middle: 2.0 mm, Bottom: 2.5 mm.

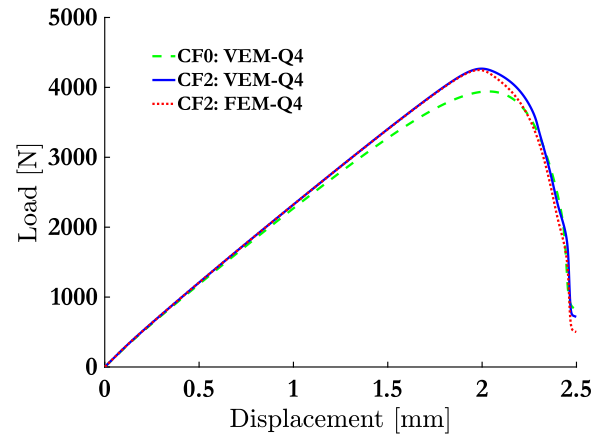


Figure 6: SEN-T: Load-Displacement curve.

4.2 Single-Edge V-Notch Specimen under Tension (SEVN-T)

In this example a single-edge V-notched specimen is considered.

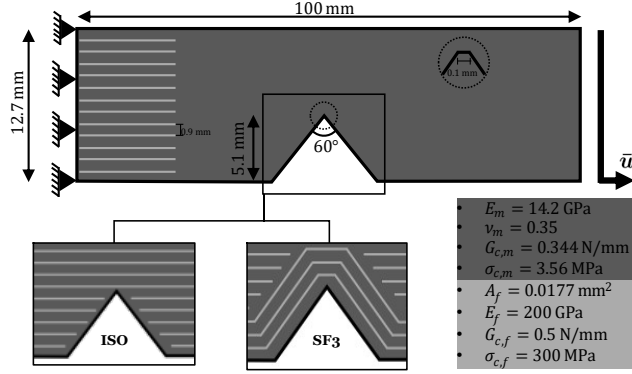


Figure 7: SEVN-T: Problem setup.

The problem geometry, boundary conditions and reinforcement scenarios are shown in Fig. 7. The first scenario, termed "ISO", considers isotropic fibre deposition along the loading direction. The second configuration, termed "SF3", considers 3 fibres around the V-notch and isotropic reinforcement for the rest of the domain. The specimen thickness is set to 3 mm. The selected mechanical and fracture properties are intended to reflect those of a layer of 3D printed concrete and reinforcing steel fibres. The specimen is subjected to tension by incrementally imposing a displacement equal to 0.05 mm on the right edge, while fixing the left. The increment is set to $\Delta u = 0.00005$ mm and the length scale to $L = 0.3$ mm. The domain is discretized with 36122 virtual elements.

Fig. 8 illustrates the response curves for the two configurations. Although the isotropic fibre layout achieves a 7% higher ultimate load, the SF3 configuration achieves a more ductile response. Fig. 9 contains the phase field contour plots for three values of the imposed displacement, namely 0.02 mm (top), 0.03 mm (middle) and 0.05 mm (bottom). The isotropic layout results in an anticipated crack pattern, i.e., the crack propagates along the axis of symmetry. However, the SF3 configuration induces anisotropic behavior. The points where the fi-

bres are tessellated result in stress concentrations that enforces the crack propagate towards them, deviating from a straight path. Similar to the previous case, the crack is arrested on each fibre.

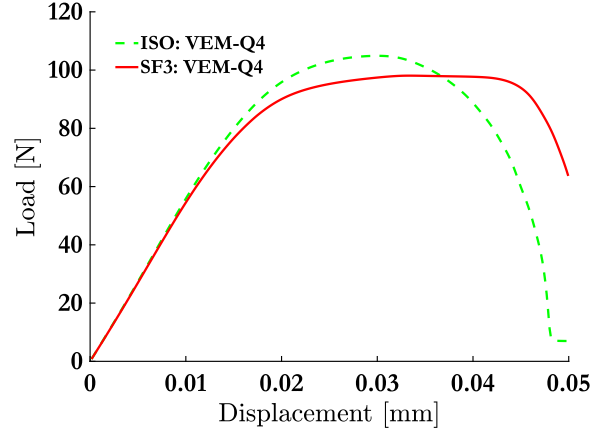


Figure 8: SEVN-T: Load-Displacement curve.

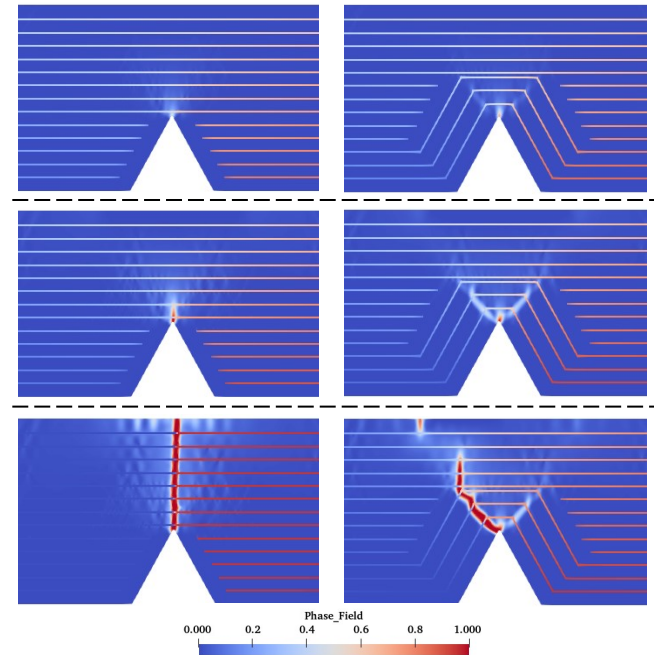


Figure 9: SEVN-T: Phase field contour plots for different top edge displacements. Top: 0.02 mm, Middle: 0.03 mm, Bottom: 0.05 mm.

5 Conclusions

In this work a cohesive fracture phase field model is incorporated with the Virtual Element Method to simulate continuous fibre reinforced

composite specimens. The fibres are modeled using an embedded element technique. This offers an advantage, in terms of simplicity, over traditional homogenization techniques, as there is no need to calculate equivalent orthotropic properties for the reinforced specimens. The numerical benchmarks demonstrate the effectiveness of the proposed framework in accurately capturing fracture evolution in reinforced domains. Both ultimate strength increase as well as fibre-induced anisotropy were captured.

Acknowledgments

The research project is implemented in the framework of H.F.R.I call “Basic research Financing (Horizontal support of all Sciences)” under the National Recovery and Resilience Plan “Greece 2.0” funded by the European Union –NextGenerationEU (H.F.R.I. Project Number: 15097).

REFERENCES

- [1] Francfort, G., Marigo, J.J. 1998. Revisiting brittle fracture as an energy minimization problem. *Journal of the Mechanics of Physics of Solids* **46**(8):1319-1342.
- [2] Lukaszewicz, D.H.J.A., Ward, C., Potter, K.D. 2012. The engineering aspects of automated prepreg layup: History, present and future. *Composites Part B: Engineering* **43**: 997-1009.
- [3] Kabir, S.M.F, Mathur, K., Seyam, A.F.M. 2020. A critical review on 3D printed continuous fiber-reinforced composites: History, mechanism, materials and properties. *Composite Structures* **232**:111476.
- [4] ISO/ASTM: ISO/ASTM 52900:2021 - Additive Manufacturing - General principles - Fundamentals and vocabulary. 2021. Accessed: Nov. 11, 2024. [Online].
- [5] Brenken, B., Barocio, E., Favaloro, A., Kunc, V., Pipes, R.B. 2018. Fused filament fabrication of fiber-reinforced polymers: A review. *Additive Manufacturing* **21**:1-16.
- [6] Mashayekhi, F., Bardon, J., Berthé, V., Perrin, H., Westermann, S., Addiego, F. 2021. Fused filament fabrication of polymers and continuous fiber-reinforced polymer composites: Advances in structure optimization and health monitoring *Polymers* **13**(5):789.
- [7] Saeed, K., McIlhagger, A., Harkin-Jones, E., Kelly, J. 2021. Predication of the in-plane mechanical properties of continuous carbon fibre reinforced 3D printed polymer composites using classical laminated-plate theory *Composite Structures* **259**:113226.
- [8] Pillai, U., Triantafyllou, S.P., Essa, Y., de la Escalera, F.M. 2020. An anisotropic cohesive phase field model for quasi-brittle fractures in thin fibre-reinforced composites *Composite Structures* **252**:112635.
- [9] Geelen, R.J.M., Liu, Y., Hu, T., Tupek, M.R., Dolbow, J.E. 2019. A phase-field formulation for dynamic cohesive fracture. *Computer Methods in Applied Mechanics and Engineering* **348**:680-711.
- [10] Pham, K., Amor, H., Marigo, J.J., Maurini, C. 2011. Gradient damage models and their use to approximate brittle fracture. *International Journal of Damage Mechanics* **20**(4):618-652.
- [11] van Dijk, N.P., Espadas-Escalante, J.J., Isaksson, P. 2020. Strain energy density decompositions in phase-field fracture theories for orthotropy and anisotropy. *International Journal of Solids and Structures* **196-197**:140-153.
- [12] Miehe, C., Hofacker, M., Welschinger, F. 2010. A phase field model for rate-independent crack propagation: robust algorithmic implementation based on operator splits. *Computer Method in Applied Mechanics and Engineering* **199**(45-48):2765-2778.

- [13] Lorentz, E. 2017. A nonlocal damage model for plain concrete consistent with cohesive fracture. *International Journal of Fracture* **207**:123-159.
- [14] Reddy, J.N. 2013. *An Introduction to Continuum Mechanics*. Cambridge University Press, New York (2nd ed.).
- [15] Courant, R., Hilbert, D. 1953. *Methods of Mathematical Physics* (Vol. 1). Interscience Publishers Inc., New York (1st ed.).
- [16] Antonietti, P.F., Beirão da Veiga, L., Manzini, G. 2022. *The Virtual Element Method and its Applications*. Vol. 31 of SEMA SIMAI Springer Series. Springer Nature, Switzerland AG.
- [17] Wriggers, P., Aldakheel, F., Hudobivnik, B. 2024. *Virtual Element Methods in Engineering Sciences*. Springer Nature, Berlin.
- [18] Beirão da Veiga, L., Brezzi, F., Marini, L. 2013. Virtual elements for linear elasticity problems. *SIAM, Journal of Numerical Analysis* **51**:794-812.
- [19] Wheeler, M.F., Wick, T., Wollner, W. 2014. An augmented-Lagrangian method for the phase-field approach for pressurized fractures. *Computer Methods in Applied Mechanics and Engineering* **271**:69-85.
- [20] Aldakheel, F., Hudobivnik, B., Hussein, A., Wriggers, P. 2018. Phase-field modelling of brittle fracture using an efficient virtual element scheme. *Computer Methods in Applied Mechanics and Engineering* **341**:443-466.
- [21] Liu, T.R., Aldakheel, F., Aliabadi, M.H. 2023. Virtual element method for phase field modeling of dynamic fracture. *Computer Methods in Applied Mechanics and Engineering* **411**:116050.
- [22] Wriggers, P., Reddy, B., Hudobivnik, B. 2017. Efficient virtual element formulations for compressible and incompressible finite deformations. *Computational Mechanics* **60**:253-268.
- [23] Berg, M., Cheong, O., Kreveld, M., Overmars, M. 2008. *Computational Geometry: Algorithms and Applications*. Springer Verlag, USA, (3rd ed.).
- [24] Bathe, K.J. 2014. *Finite element procedure*. Prentice Hall. (2nd ed.).
- [25] Avanzini, A., Battini, D., Giorleo, L. 2022. Finite element modelling of 3D printed continuous carbon fiber composites: Embedded elements technique and experimental validation. *Composite Structures* **292**:115631.
- [26] <https://markforged.com/resources/blog/reinforcing-3d-printed-parts-part-1>. Accessed: Dec. 10, 2024. [Online]
- [27] Katsikadelis, J.T. 2020. *Dynamic Analysis of Structures..* Academic Press, (1st ed.).
- [28] <https://markforged.com>. Accessed: Dec. 10, 2024. [Online]
- [29] Sangaletti, S., García, I.G. 2022. Fracture Tailoring in 3D printed continuous fibre composite materials using the Phase field approach for fracture. *Composite Structures* **300**:116127.
- [30] Chacón, J.M. *et al.* 2019. Additive manufacturing of continuous fibre reinforced thermoplastic composites using fused deposition modelling. Effect of process parameters on mechanical properties. *Composites Science and Technology* **181**:107688.
- [31] Saeed, K. *et al.* 2021. Predication of the in-plane mechanical properties of continuous carbon fibre reinforced 3D printed polymer composites using classical laminated-plate theory. *Composite Structures* **259**:113226.